Materials Horizons

ROYAL SOCIETY OF CHEMISTRY

COMMUNICATION

View Article Online
View Journal | View Issue

Cite this: *Mater. Horiz.*, 2025, **12**, 3444

Received 24th December 2024,
Accepted 17th February 2025

DOI: 10.1039/d4mh01896f

rsc.li/materials-horizons

Droplet-templating soft materials into structured bead-based aerogels with compartmentalized or welded configurations†

Shayan Ghasemi,‡[a] Mahyar Panahi-Sarmad, ‡[bc] Elnaz Erfanian,[ac] Tianyu Guo, [c] Vahid Rad, [d] Adel Jalaee, [c] Gabriel Banvillet, [c] E. Johan Foster, [c] Kam C. Tam, [a] Masoud Soroush, [d] Feng Jiang, [c] Orlando J. Rojas [bce] and Milad Kamkar *[a]

Achieving precise control over the composition and architecture of nanomaterial-based aerogels remains a significant challenge. Here, we introduce a droplet-templating approach to engineer ultra-lightweight aerogels *via* the interfacial co-assembly of nanoparticles-surfactants (NPSs) at polar/apolar liquid interfaces. This approach enables the creation of aerogels with tailored compartmentalized or welded bead architectures, exhibiting multilayer, gradient, and hybrid morphologies from a range of 1D and 2D nanomaterials. By precisely controlling evaporation and freeze-drying processes, we fabricate aerogels with customizable micro-domains, without requiring chemical binders. Our approach provides a platform for developing soft materials with tunable properties, paving a new path for applications in soft matter and aerogel engineering.

New concepts

We introduce a new route to soft matter engineering *via* interfacial co-assembly of nanomaterials to fabricate structured aerogels—including hybrid, multilayer, and gradient forms—using a wide range of 1D and 2D nanomaterials. They are achieved through a precisely controlled, yet simple method, herein coined "droplet-templating". This approach overcomes a key challenge in hybrid aerogel synthesis, specifically in managing the composition and the precise localization of components/nanomaterials. Through droplet-templating, we also introduce two innovative types of aerogels based on compartmentalized and welded bead architectures, each characterized by distinct nano/micron-scale domains. Our approach broadens the possibilities for soft matter engineering, offering enhanced functionality and applicability across a wide range of applications.

1. Introduction

The interfacial co-assembly and jamming of nanomaterials at liquid–liquid interfaces sets a new route for the fabrication of soft functional materials, where the nanoparticles' characteristics are transferred to macroscopic products.[1–3] Interfacial jamming involves the interaction between functionalized nanoparticles dispersed in one liquid and polymeric or oligomeric ligands dissolved in another immiscible phase, forming nanoparticles-surfactants (NPSs).[4–7] This technique enables the fabrication of soft materials known as structured liquids that are easy to flow but are able to shape like solids due to an interfacial layer between two liquids.[1] Moreover, it offers a pathway to overcome the challenges imposed by complex rheological behaviors (baths and inks) during printing, such as direct ink writing, providing full control over hybrid soft material composition, structure, function, and architecture.[1,2,8,9]

One critical application of structured liquids is their use as templates for aerogel fabrication, allowing programmable control over the density, porosity, and structural features of aerogels at micro- to mesoscale.[10–13] However, current research into structured liquid templates has not yet established a universal method for producing aerogel beads. Beads are easily handled, transformed and stored, and hold promise for applications in sensors, electronics, environmental remediation, and beyond.[10,14–16] Furthermore, by leveraging the versatility of structured liquids, customized liquid droplet templates can be formed, enabling the creation of multilayer, hybrid, and gradient stable emulsions or suspensions, which are ideal for producing novel ultra-lightweight aerogels.

Compared to conventional aerogel fabrication methods such as liquid marbling, droplet gelation in coagulation baths,

[a] *Department of Chemical Engineering, Waterloo Institute for Nanotechnology, University of Waterloo, 200 University Avenue West, Waterloo, Ontario N2L 3G1, Canada. E-mail: Milad.kamkar@uwaterloo.ca*
[b] *Department of Wood Science, The University of British Columbia, 2900-2424 Main Mall, Vancouver, BC V6T 1Z4, Canada*
[c] *BioProducts Institute and Department of Chemical and Biological Engineering, University of British Columbia, 2360 East Mall, Vancouver, BC V6T 1Z3, Canada*
[d] *Department of Chemical and Biological Engineering, Drexel University, Philadelphia, PA 19104, USA*
[e] *Department of Chemistry, The University of British Columbia, 2036 Main Mall, Vancouver, BC V6T 1Z1, Canada*

† Electronic supplementary information (ESI) available. See DOI: https://doi.org/10.1039/d4mh01896f

‡ These authors contributed equally to this work.

or sprayed droplet freezing, the droplet-templating approach demonstrates clear advantages.[14,17–19] Typically, these methods necessitate additional chemical or polymeric binders to ensure droplet gelation as a template for aerogel production, significantly adding to the cost and complexity of the process while impacting the density and pore distribution of the resulting aerogels.[16] Moreover, the prevalent technologies for routine aerogel bead fabrication lack universality, hindering the incorporation of diverse functional nanoparticles (NPs); they also fail to program the resultant bead-like morphologies for the production of alternative soft material systems through on-demand welding of bead-like templates. Therefore, recognizing the value of structured liquids as cost-effective and reconfigurable templates is paramount for aerogel bead fabrication.

Herein, we present a novel one-step approach for fabricating structured liquid droplets, serving as a versatile and reconfigurable template to prepare compartmentalized or welded aerogel beads. Our approach involves streaming a binder and gelation-free aqueous suspension of functional NPs into a nonpolar bath containing a surfactant. This process results in the formation of droplet-based soft materials through NPSs interfacial assembly and jamming. The versatility of this approach is demonstrated by utilizing various 1D and 2D NPs based on the final application, including $Ti_3C_2T_x$ MXene nanosheets, graphene oxide (GO) nanosheets, cellulose nanofibers (CNFs), and cellulose nanocrystals (CNCs) (Scheme 1).

The strength of our method lies in its precise control over the morphological features of the aerogels, achieved by adjusting NPs assembly. This versatility allows the production of non-associative, freely flowing droplets, as well as multilayer, hybrid, or gradient liquids, which can be transformed into compartmentalized or welded aerogel beads. All combined, this method paves the path for controlling the distribution and functionality of soft materials across nano-to-macro scales.

2. Results and discussion

2.1. Harnessing self-assembly for interfacial layer formation: droplet-templating

The fabrication of aerogel beads follows a four-step droplet-templating process: (1) the aqueous phase containing nanoparticles (NPs) jet into an immiscible liquid, such as hexane, containing surfactants (herein we used PSS-[3-(2-aminoethyl) amino]propyl-heptaisobutyl substituted POSS (POSS-NH_2)) (see Videos S1 and S2, ESI†), (2) the NPs migrate toward the interface through random motion and bond with the surfactant at the liquid–liquid interface (Fig. 1a depicts this schematically and Video S3 shows the interface, ESI†), (3) the aqueous droplets are then frozen and the liquid hexane phase is removed (Video S4 shows frozen droplets of suspensions, ESI†), (4) freeze-drying removes the ice crystals, yielding ultra-lightweight aerogel beads (Fig. S1, ESI†).[11,20] The entire process herein is called "droplet-templating". Four different types of 1D and 2D NPs, including graphene oxide (GO), $Ti_3C_2T_x$ (MXene), cellulose nanocrystals (CNCs), and cellulose nanofibers (CNFs), at 0.1–1.0 wt%, are dispersed in water (shown in Fig. S2, ESI†) and jetted for aerogel fabrication. The required concentration of the NPs or surfactants to successfully achieve stable droplets depends on the NPs' physical and chemical properties.

Although the proposed method leads to droplet/bead formation for all the mentioned NPs (Fig. S3, ESI†), the underlying assembly mechanisms at the interface vary slightly depending on the NPs.[10,11,20,21] Upon extruding the aqueous phase containing GO into the hexane/POSS-NH_2, complexation occurs at the interface, where the protonation of primary amines generates positively charged POSS-NH_3^+, reducing the interfacial energy.[4,11] Concurrently, driven by random motion, GO nanosheets that are close to the interface assembled at the water/hexane interface, aided by its amphiphilic nature.[4,11] At the interface, the deprotonated functional groups such as

Scheme 1 The proposed universal droplet-templating approach for fabricating droplet-based soft materials. This work showcases structured aerogels, based on 1D and 2D nanoparticles (CNCs, CNFs, graphene, and $Ti_3C_2T_x$ MXene), can be fabricated using this droplet-templating approach.

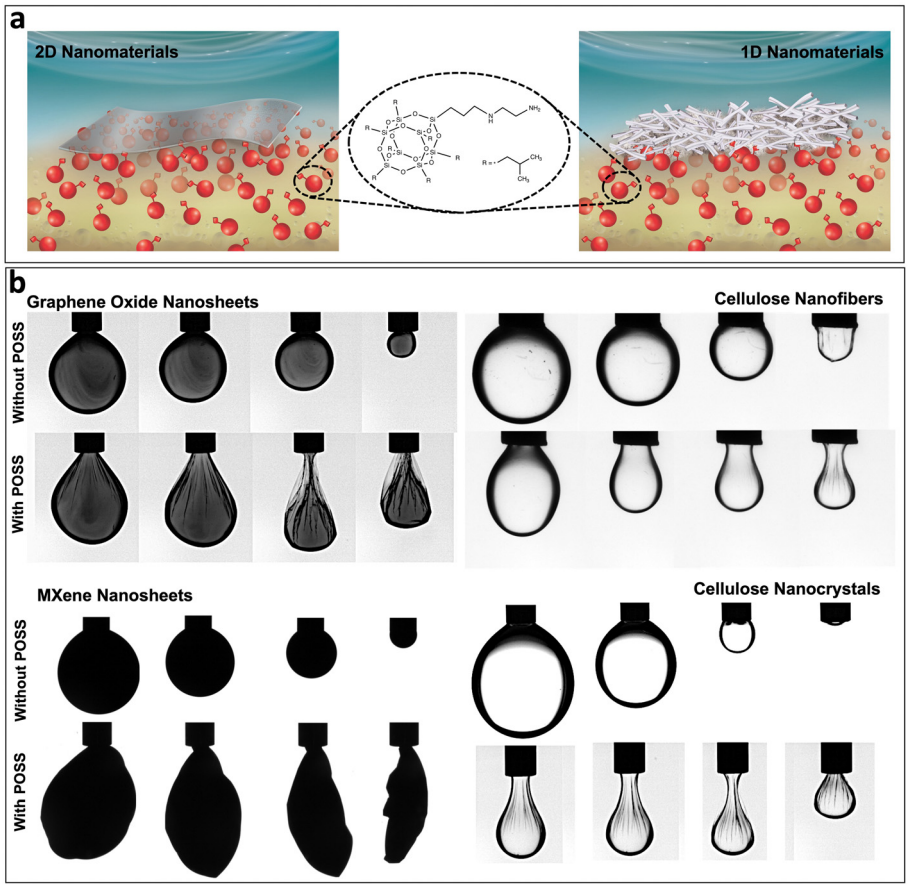

Fig. 1 (a) Schematics depicting the co-assembly of 2D nanosheets/1D nanomaterials and POSS at the oil/water interface. (b) Contraction of the pendent droplet of the aqueous phase containing different nanomaterials in the hexane phase with and without POSS. During compression, the droplet volume decreases, shrinking the interfacial area and exerting compressive forces. Videos of similar systems can be found in our previous reports such as.[7]

carboxylic acid groups (COO^-) on the GO nanosheets interact electrostatically with the positively charged POSS-NH_3^+.[4,11] The complexation between POSS and NPs drives the co-assembly of nanoparticle-surfactants (NPSs).[4,11] This cooperative assembly and jamming occur due to NP packing at the interface, which minimizes the interfacial energy,[4,11] effectively forming a solid-like layer around the aqueous droplets (Fig. 1b). This layer can be visualized in Video S3 (ESI†), and its solid nature can be ascertained by the pendent-droplet test. Detailed descriptions of the assembly mechanisms for other nanomaterials, such as MXenes, CNCs, and CNFs, are provided in the ESI.†

We conducted pendant drop experiments to assess the influence of POSS on interfacial layer formation.[10] Various nanomaterials dispersed in the water phase were pumped into and then withdrawn from the oil phase (expansion–contraction), with and without POSS. As shown in Fig. 1b, in the absence of POSS, NPs partially jammed at the hexane–water interface, resulting in the formation of a weak interfacial layer. Thus, during the evacuation of the pendant drops, the droplets exhibited shrinkage without any wrinkles, clarifying the lack of sufficient robustness in the interfacial layers.[21] In contrast, with the incorporation of POSS, a robust interfacial layer was formed, as evidenced by the appearance of wrinkles during the withdrawal process.

This observation presents compelling evidence of a robust interfacial layer formation at the interface, capable of effectively reducing the interfacial tension. This indicates that POSS (see Fig. 1b) exhibits a strong interaction with these NPs, owing to its potential to form a strong interaction with GO, CNCs, CNFs, and $Ti_3C_2T_x$. Among these NPs, the droplet surface of GO and the MXene displays more wrinkles compared to those of CNCs and CNFs. This serves as clear-cut evidence that the planar shape (2D) of these NPs effectively traps them at the interface due to their geometrical and amphiphilic features.[12,22] In contrast, for fiber/rod-shaped (1D) NPs such as CNFs and CNCs, the wrinkles were less noticeable, indicating the better robustness of the interfacial layers formed by the 2D NPs.

This is further confirmed by equilibrium interfacial tension (IFT). The IFT of water/hexane was found to be ≈ 52 mN m^{-1} and it dropped to approximately 47 ± 1 and 33 ± 2 mN m^{-1} in the presence of $Ti_3C_2T_x$ and GO, respectively. Across all types of studied NPs, the addition of POSS significantly reduced IFT values. Particularly, the effectiveness of POSS was most pronounced in assembly with $Ti_3C_2T_x$ nanosheets, where IFT decreased from approximately 47 ± 1 mN m^{-1} to around

3 ± 1 mN m^{-1}. The successful $Ti_3C_2T_x$–POSS co-assembly can be attributed to the electrostatic interactions between the amine groups of POSS and the functional groups of $Ti_3C_2T_x$, alongside its 2D shape.[23] A similar trend was observed for GO nanosheets, where IFT decreased from 33 ± 2 mN m^{-1} to 3.5 ± 1 mN m^{-1}. This demonstrates the benefit of 2D nanostructures in forming robust interfacial layers. Additionally, GO alone reduced the IFT of the water/hexane interface from ≈ 52 mN m^{-1} to 33 ± 2 mN m^{-1}, reflecting its amphiphilic nature.[24]

The incorporation of POSS into systems containing CNCs and CNFs also led to significant reductions in IFT. For CNCs, the equilibrium IFT decreased from 40 ± 2 mN m^{-1} to approximately 3 ± 1 mN m^{-1} in the presence of POSS. Similarly, for CNFs, the IFT dropped from 34 ± 2 mN m^{-1} to 7 ± 1 mN m^{-1} upon the addition of POSS. This suggests that the proposed approach is effective in reducing IFT and creating stable interfacial layers in the case of various NPs (nanosheets, nanocrystals, and nanofibers), confirming its universality. This strategy provides a versatile platform for engineering functional interfaces with tailored properties, enabling diverse applications.

A novel yet simple test was designed to visualize the formation of the NPSs films. As shown in Fig. 2a, a layer of hexane containing POSS was placed on the surface of an aqueous GO suspension. As the hexane layer gradually evaporated, a solid layer began to form, progressing from the edge of the container toward the center. Upon complete evaporation of the hexane, a solid and well-formed layer was obtained (as shown in Fig. 2a). This demonstrates the capability of the interfacial layer to develop and maintain its structure independently of the surrounding medium, whether in a confined or isolated system.[21,25,26]

We successfully produced compartmentalized all-aqueous liquids using this technique, as shown in Fig. 2b. The black phase represents an aqueous GO suspension, while the transparent phase represents an aqueous CNC suspension. To achieve compartmentalization, we first formed an NPSs layer on the CNC suspension, following the process outlined in Fig. 2a. A GO

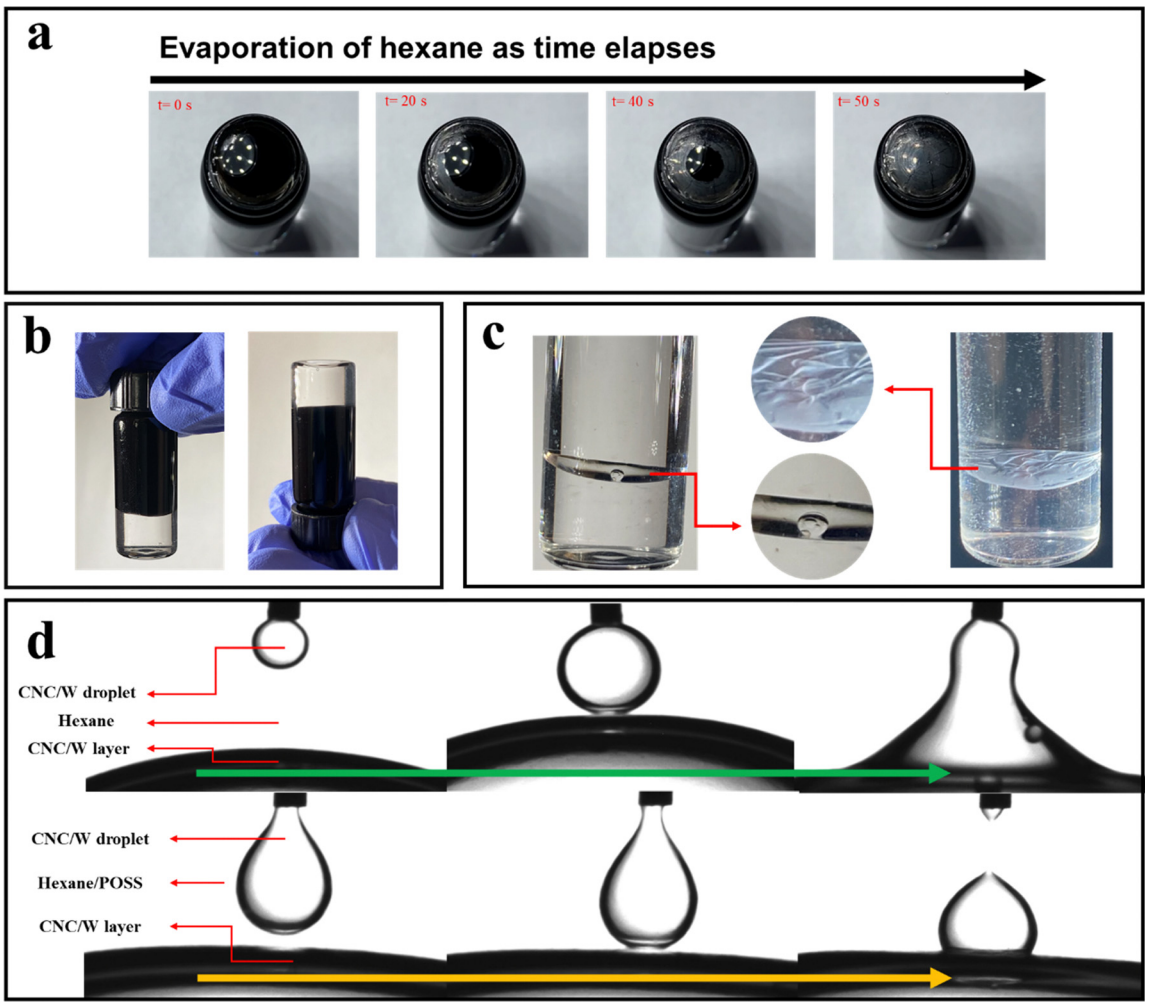

Fig. 2 (a) GO-POSS NPSs layer formation during hexene evaporation, with the layer generation process lasting approximately 50 seconds in a vial (width ≈ 16.4 mm, height ≈ 47.6 mm). (b) Compartmentalized all-aqueous GO and CNC suspensions in a vial (width ≈ 16.4 mm, height ≈ 47.6 mm). (c) CNC suspension droplet stability on top of the CNC suspension/hexane–POSS interface immediately after interface formation and after a week in a vial (width ≈ 24.6 mm, height ≈ 48.4 mm). (d) Droplet stability at the interface of CNC suspension/hexane in the presence (bottom) and absence (top) of POSS in the hexane phase, process lasting approximately 45 seconds.

suspension was then gently added to the top. The robust CNC-POSS NPSs layer acted as a barrier, preventing mixing between the aqueous phases, even when the vial was inverted (Fig. 2b). Furthermore, the interfacial layer is robust enough to prevent the diffusion of the NPs. A compartmentalized all-CNC suspension is depicted in Fig. S4 (ESI†). Since both layers are transparent, the top layer has been marked by a fluorescent color, confirming successful compartmentalization.

Fig. 2c further validates the robustness of NPSs films at the interface of a transparent hexane-POSS (top phase)/CNC (bottom phase) suspension. After forming an NPS interfacial film between the CNC suspension (bottom phase) and hexane–POSS (top phase)—similar to the interfaces observed in Video S3 (ESI†)—a CNC suspension droplet was placed upon the interfacial layer. Despite the CNC suspension being the same in both the bottom phase and the droplet, the NPSs interfacial film effectively prevented coalescence. Video S5 in the ESI† confirms that non-attractive interactions exist among the NPSs surrounding the droplet and between the liquids, allowing the droplet to roll on top of the interface freely.

Fig. 2d illustrates the strength of the NPSs interfacial layer with and without the inclusion of POSS. In the top row of Fig. 2d, the hexane phase lacks POSS, while in the bottom row, it contains POSS (with the CNC suspension serving as the bottom phase, similar to the conditions depicted in Video S3, ESI†). A pendant droplet of CNC suspension was then formed in the top phase in both scenarios and slowly lowered to touch the interface. Without POSS (Fig. 2d, top row), the aqueous CNC droplet immediately merged into the bottom aqueous CNC suspension phase upon contact. Conversely, in the presence of POSS (Fig. 2d, bottom row), the droplet remained stable even after touching the bottom layer, which has a composition identical to the droplet. This stability is attributed to the formation of a strong NPSs interfacial layer on the base layer surrounded by the droplet. The robustness of this interfacial layer enables it to act as an effective barrier, preventing the droplets from merging with the bottom phase.[27] This observation motivated us to propose a range of novel soft materials and ultra-lightweight aerogels in the next sections.[13,28]

2.2. Bead and interfacially welded micro-aerogels by droplet-templating

As discussed, the fabrication of NP-loaded droplets involves jetting the suspensions into a hexane–POSS bath (see Videos S1 and S2 for the processes with GO and $Ti_3C_2T_x$, respectively, ESI†). Upon jetting the ink into the bath, the droplets reshape and are stabilized by a robust interfacial layer—a process referred to as droplet-templating. The break-up of the continuously jetted stream into individual droplets is governed by Rayleigh–Plateau instabilities, which are caused by surface tension forces that create growing perturbations along the jet, eventually breaking it into droplets to minimize surface energy.[29] Several factors, including the flow rate and needle size, play critical roles in controlling the size of the droplets.[4] The relationship between the droplet size and the parameters of flow rate, needle size, and injection pressure can be explained using principles of fluid dynamics. The flow rate Q depends on the injection pressure (ΔP), needle radius (r), needle length (L), and fluid viscosity (η) according to the Hagen–Poiseuille equation: $Q = \pi r^4 \Delta P / 8\eta L$. The droplet volume V is directly proportional to Q, and the detachment frequency $f = Q/V$. Assuming a spherical droplet, the diameter (D) of the droplets can be estimated from $D = (6Q/\pi f)^{1/3}$ in dripping regime. For a needle with an inner diameter of 0.26 mm and a length of 8.6 mm, and a fluid with the viscosity of water, flow rates were calculated for different pressures. For instance, at 150 kPa, the flow rate was 117.38 mL min^{-1}, while at 50 kPa, it was 39.13 mL min^{-1}. However, in the jetting regime, increasing Q increases the jet velocity, which subsequently reduces the dominant breakup wavelength of the liquid stream. This occurs due to Rayleigh–Plateau instability, which causes the jet to break into smaller droplets at higher flow rates. As the velocity increases, the instability grows more rapidly, leading to more frequent droplet formation and a reduction in droplet size. Consequently, at a fixed needle size, higher flow rates (pressures) result in the generation of smaller droplets in the jetting regime. Thus, as the flow rate increased by raising the injection pressure, the average droplet diameter decreased progressively (from $\approx$796 μm at 50 kPa to $\approx$510 μm at 100 kPa and $\approx$268 μm at 150 kPa, as depicted in Fig. 3a). Similar behavior was observed for other NPs (Fig. S5 and S6 (ESI†)). The droplets formed during the injection process exhibited remarkable stability regardless of their size; they did not adhere to one another, and no coalescence occured (see Videos S6 and S7, ESI†). The robust interfacial layer maintains the spherical shape of the droplets, even when subjected to stress from other droplets (as demonstrated in Fig. S5, ESI†). In addition, we demonstrated the bulk movement of the droplets (see Video S7a, ESI†), confirming the non-attractive nature of the interfacial NPSs layer. This feature, along with the strength of the interfacial layer, makes the droplets transferable (see Video S7b, ESI†), expanding the application range of these novel soft materials. Moreover, the ability to fabricate these droplets from different NPs further widens their versatility and potential applications.

Upon freeze-drying these stabilized droplets, aerogel beads were produced. Interestingly, through controlled evaporation of the continuous hexane phase (Video S8, ESI†), we fabricated interfacially compartmentalized or welded droplets, leading to the corresponding aerogels (see optical images in Fig. 3b). During the initial stage of evaporation, the droplets remained stable, and in the later stages, the welding of these droplets becomes evident. However, the distinct boundaries between the domains remain recognizable, as illustrated in Fig. 3b. The SEM images in Fig. 3b reveal the aerogels formed at different stages of evaporation.

Videos S8–S10 (ESI†) demonstrate that this process can be achieved for all NPs and even hybrid systems. As mentioned, even after hexane evaporation, the boundary remains strong enough to prevent droplet merging (see Videos S8–S10, ESI†). As shown in Video S10 (ESI†), hybrid structures maintain their individual domains during the evaporation of hexane, with only

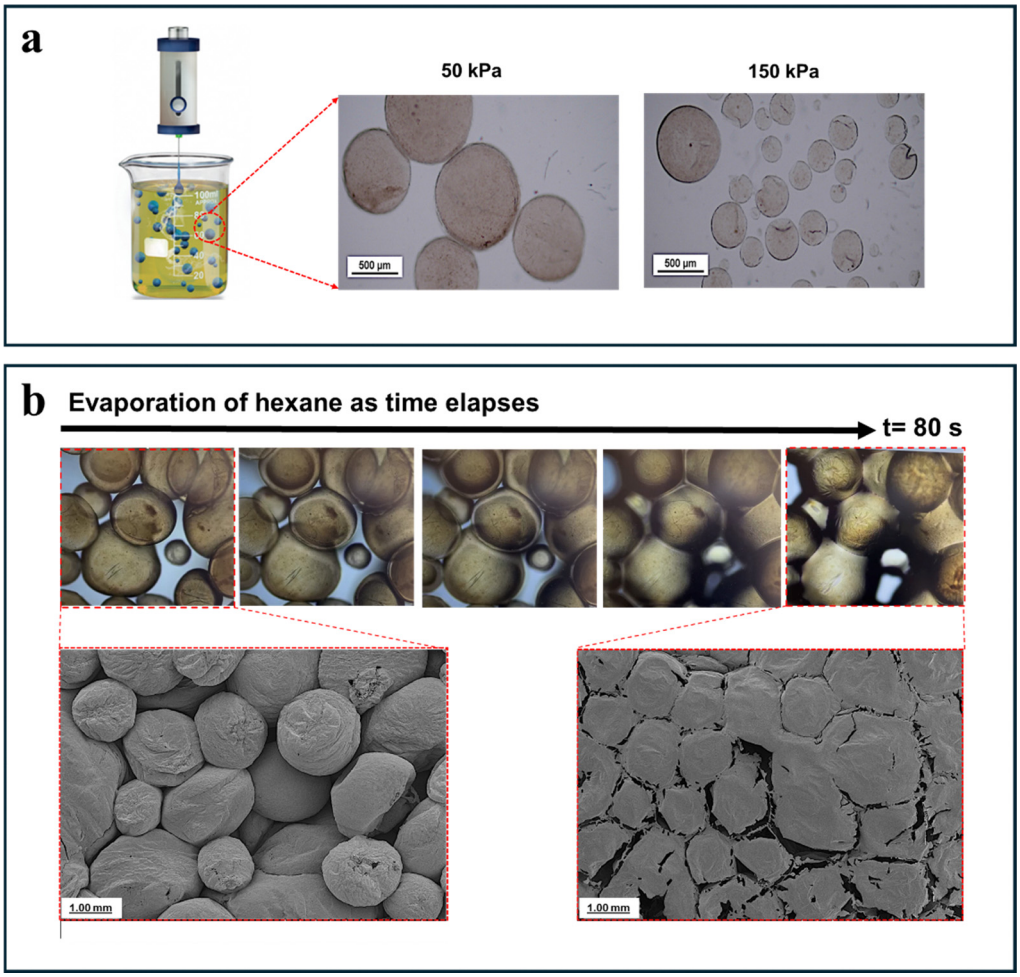

Fig. 3 (a) Optical microscopy photos exhibiting the diameter tunability of the droplet with the injection rate. (b) Optical microscopy images showing the morphological evolution of the GO droplets during hexane evaporation, and SEM images revealing the respective aerogels formed at different stages of hexane evaporation.

droplet adhesion observed. This presents a unique opportunity to introduce innovative hybrid aerogels with micro-domains consisting of different NPs.

2.3. Layers, gradients, and hybrid soft materials and their resultant aerogels

In advanced porous structures, creating hybrid aerogels to achieve multifunctionality is an arduous challenge.[30–33] Indeed, as the precursors for the fabrication of ultra-lightweight aerogels are liquid-like soft materials, achieving layered, gradient, or hybrid aerogels with controlled nano-, micro-, and macro-scale domain composition/morphology has yet to be realized. The remarkable stability of the droplets, as shown in the previous section, allows for the fabrication of diverse droplet-based soft materials *via* the facile and simple droplet-templating technique.

Fig. 4a shows the formation of single-layer $Ti_3C_2T_x$ MXene droplet-based soft materials. Fig. 4b and c and Video S11 (ESI†) illustrate the formation of multilayer all-liquid droplet-based soft materials, demonstrating the capability to produce complex architectures with multiple distinct layers. These layers can consist of any arbitrary combination of $Ti_3C_2T_x$ MXene, GO, CNC, or CNF droplet-based soft materials, as illustrated in Fig. 4a–d. Mixing these layered structures achieves a transition from a layered to a heterogeneous hybrid architecture, effectively combining $Ti_3C_2T_x$, GO, CNCs, and CNFs droplets (Fig. 4f and Video S12, ESI†). The excellent interfacial assembly within the hybrid structure ensures that all droplets, regardless of their nanomaterial components, maintain their shapes even during mixing and bulk movement. In this regard, Fig. 4d demonstrates the creation of a gradient CNC/MXene all-liquid soft material. This gradient structure is achieved by pre-mixing CNC and MXene droplets in different ratios and then layering them sequentially on top of each other. This gradient formation illustrates the versatility of the droplet-templating technique in designing materials with gradual transitions in composition and properties.

By a simple one-step freeze-drying of the mentioned soft materials, aerogels with any specific composition can be achieved. Controlled evaporation of hexane before freeze drying

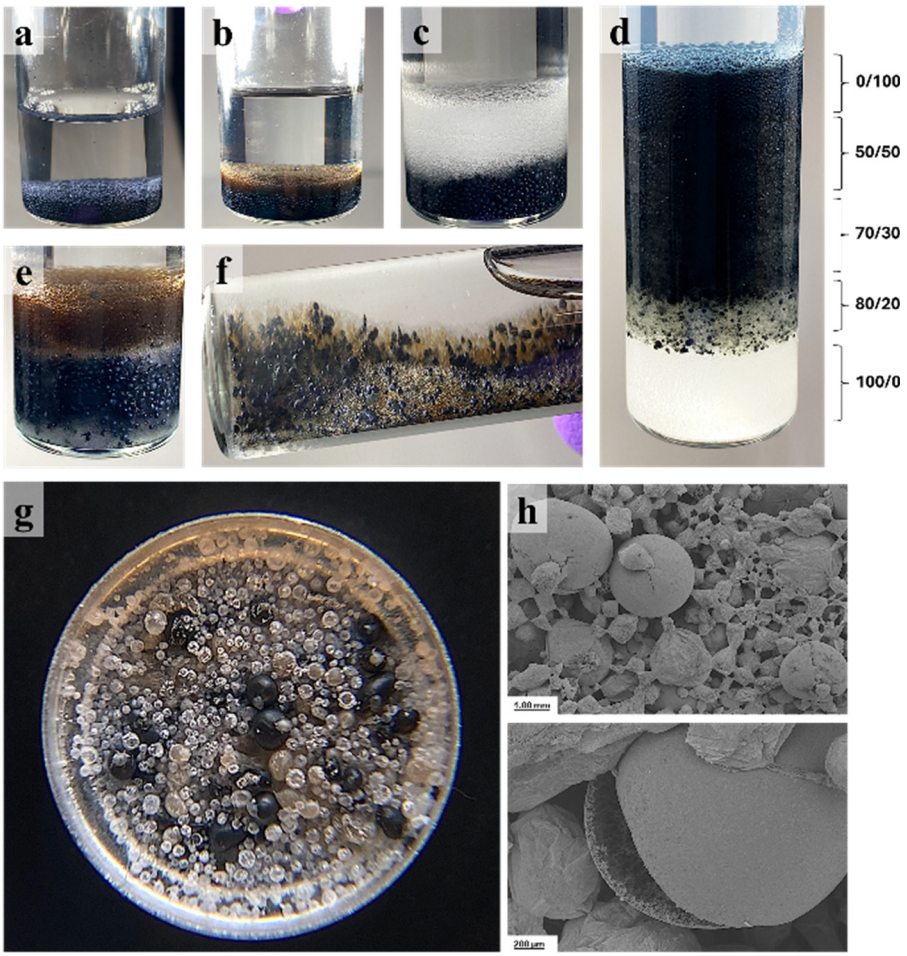

Fig. 4 (a) A layer of $Ti_3C_2T_x$ MXene droplet in a vial (width ≈ 24.6 mm, height ≈ 48.4 mm). (b) Multilayer droplet-templated soft materials (bottom layer: MXene droplets and top layer: GO droplets) in a vial (width ≈ 24.6 mm, height ≈ 48.4 mm). (c) Multilayer droplet-templated soft materials (bottom layer: MXene droplets and top layer: CNC droplets) in a vial (width ≈ 24.6 mm, height ≈ 48.4 mm). (d) Gradient droplet-templated soft material: MXene and CNC layers with various compositions in each layer in a vial (width ≈ 20.4 mm, height ≈ 73.6 mm). (e) Multilayer droplet-templated soft material (bottom layer: hybrid CNC and MXene droplets and top layer: GO droplets) in a vial (width ≈ 24.6 mm, height ≈ 48.4 mm). (f) Hybrid droplet-templated soft material, consisting of the MXene, CNC, CNF, and GO droplets in a vial (width ≈ 24.6 mm, height ≈ 48.4 mm). (g) Digital images of hybrid aerogels composed of the MXene, CNC, CNF, and GO aerogel beads; the diameter of the pan is ≈ 100 mm. (h) SEM images of the MXene, CNC, CNF, and GO hybrid aerogel beads.

also allows us to produce these aerogels in the form of compartmentalized or welded beads. As a proof of concept, digital and SEM images in Fig. 4g and h demonstrate a hybrid aerogel resulting from freeze-drying hybrid $Ti_3C_2T_x$, GO, CNC, and CNF droplets. The integration of aerogel beads into hybrid compartmentalized or welded systems presents unique possibilities and advantages.

By combining different NPs into layered or heterogeneous structures, this approach offers exceptional versatility and precise control over the composition and properties of the resulting hybrid aerogels. The remarkable stability, structural diversity, and preserved morphology of these hybrid beads make them highly promising for a wide range of applications, including biotechnology, soft robotics, and energy storage.[34–37] These beads can also be loaded with other materials as cargo or actuatable materials. For instance, Video S13 and Fig. S7 (ESI†) show GO droplets loaded with magnetic particles ordered in specific shapes, such as letters by magnets.

Conclusions

This study introduced a novel droplet-templating method for designing aerogels with complex compositions. We demonstrated the fabrication of multilayer, gradient, and hybrid all-liquid droplet-based soft materials through the interfacial co-assembly of nanoparticles and surfactants at liquid–liquid interfaces. This technique enables the formation of compartmentalized or welded aerogel beads *via* controlled room-temperature evaporation of the apolar phase, followed by freeze-drying of the aqueous phase. By precisely controlling the composition, order, and morphology of these soft materials, we achieved aerogels with arbitrary micro-domain compositions,

addressing a key challenge in the field. The observed stability of these aerogels across various compositions and drying methods highlights the robustness of the droplet-templating approach. This method allows for customizing aerogel properties, paving the way for applications in energy storage, catalysis, environmental remediation, and beyond.

Author contributions

M. K. and S. G. conceived the project. S. G. and M. P. S. conducted the experimental work and wrote the manuscript. E. E., O. J. R., K. C. T., and F. J., participated in discussions. T. G. conducted the SEM imaging. E. E., G. B., A. J., V. R., M. S., and E. J. F. assisted with nanomaterial synthesis. M. K. oversaw the project. All authors discussed the results and made contributions to the manuscript.

Data availability

The data supporting this article have been included as part of the ESI.†

Conflicts of interest

The authors declare no conflicts of interest.

Acknowledgements

M. K. acknowledges the support of the NSERC Discovery Grant, RGPIN-2023-03466. V. R. and M. S. would like to acknowledge financial support from the U.S. National Science Foundation (CMMI-2134607). Any opinions, findings, and conclusions or recommendations expressed in this material are those of the authors and do not necessarily reflect the views of the National Science Foundation.

References

1 S. Shi and T. P. Russell, *Adv. Mater.*, 2018, **30**(44), 1800714.
2 B. Wang, B. Yin, Z. Zhang, Y. Yin, Y. Yang, H. Wang, T. P. Russell and S. Shi, *Angew. Chem.*, 2022, **134**(10), e202114936.
3 X. Liu, *et al.*, *Science*, 2019, **365**(6450), 264.
4 M. Kamkar, *et al.*, *Small*, 2022, 2200220.
5 S. Zhao, *et al.*, *Nano Lett.*, 2022, **22**(13), 5538.
6 J. Forth, *et al.*, *Adv. Mater.*, 2018, **30**(16), 1707603.
7 M. Kamkar, *et al.*, *Adv. Mater. Interfaces*, 2021, 2101659.
8 Y. Yang, Z. Xia, Y. Luo, Z. Wu, S. Shi and T. P. Russell, *Supramol. Mater.*, 2022, 100013.
9 C. Huang, Z. Sun, M. Cui, F. Liu, B. A. Helms and T. P. Russell, *Adv. Mater.*, 2016, **28**(31), 6612.
10 S. A. Hashemi, *et al.*, *Adv. Mater.*, 2023, 2302826.
11 A. Ghaffarkhah, *et al.*, *Adv. Funct. Mater.*, 2023, 2304748.
12 A. Ghaffarkhah, *et al.*, *Nat. Commun.*, 2023, **14**(1), 7811.
13 S. Rostami, A. Ghaffarkhah, A. Isari, S. A. Hashemi and M. Arjmand, *Mater. Adv.*, 2023, **4**(13), 2698.
14 A. Ouyang, A. Cao, S. Hu, Y. Li, R. Xu, J. Wei, H. Zhu and D. Wu, *ACS Appl. Mater. Interfaces*, 2016, **8**(17), 11179–11187.
15 J. Li, *et al.*, *ACS Appl. Mater. Interfaces*, 2022, **14**(44), 50266.
16 W. Shi, Y. C. Ching and C. H. Chuah, *Int. J. Biol. Macromol.*, 2021, **170**, 751.
17 X. Wang, G. Li, G. Hong, Q. Guo and X. Zhang, *ACS Appl. Mater. Interfaces*, 2017, **9**(47), 41323.
18 X. Zhao, W. Yao, W. Gao, H. Chen and C. Gao, *Adv. Mater.*, 2017, **29**(35), 1701482.
19 C. Tang, P. Brodie, Y. Li, N. J. Grishkewich, M. Brunsting and K. C. Tam, *Chem. Eng. J.*, 2020, **392**, 124821.
20 S. Shi, B. Qian, X. Wu, H. Sun, H. Wang, H. B. Zhang, Z. Z. Yu and T. P. Russell, *Angew. Chem., Int. Ed.*, 2019, **58**(50), 18171.
21 H. Honaryar, S. Amirfattahi and Z. Niroobakhsh, *Small*, 2023, **19**(16), 2206524.
22 A. W. Kuziel, K. Z. Milowska, P. L. Chau, S. Boncel, K. K. Koziol, N. Yahya and M. C. Payne, *Adv. Mater.*, 2020, **32**(34), 2000608.
23 Z. Sheng, Z. Liu, Y. Hou, H. Jiang, Y. Li, G. Li and X. Zhang, *Adv. Sci.*, 2023, **10**(9), 2205762.
24 N. Yousefi, X. Lu, M. Elimelech and N. Tufenkji, *Nat. Nanotechnol.*, 2019, **14**(2), 107–119.
25 P. Gu, X. Luo, S. Zhou, D. Wang, Z. Li, Y. Chai, Y. Zhang, S. Shi and T. P. Russell, *Angew. Chem., Int. Ed.*, 2023, **62**(36), e202303789.
26 W. Feng, Y. Chai, J. Forth, P. D. Ashby, T. P. Russell and B. A. Helms, *Nat. Commun.*, 2019, **10**(1), 1095.
27 J. Forth, P. Y. Kim, G. Xie, X. Liu, B. A. Helms and T. P. Russell, *Adv. Mater.*, 2019, **31**(18), 1806370.
28 S. J. Yeo, M. J. Oh and P. J. Yoo, *Adv. Mater.*, 2019, **31**(34), 1803670.
29 P. Bazazi, H. A. Stone and S. H. Hejazi, *Nat. Commun.*, 2022, **13**(1), 4162.
30 O. V. Kharissova, C. E. Ibarra Torres, L. T. González and B. I. Kharisov, *Ind. Eng. Chem. Res.*, 2019, **58**(36), 16258.
31 Z. Zheng, H. Liu, D. Wu and X. Wang, *Chem. Eng. J.*, 2022, **440**, 135862.
32 Z. Guo, P. Ren, J. Wang, X. Hou, J. Tang, Z. Liu, Z. Chen, Y. Jin and F. Ren, *Chem. Eng. J.*, 2023, **451**, 138667.
33 J. D. Afroze, L. Tong, M. J. Abden and Y. Chen, *Adv. Compos. Hybrid Mater.*, 2023, **6**(1), 18.
34 Y. Wu, *et al.*, *Nat. Commun.*, 2015, **6**(1), 6141.
35 H. Sun, Z. Xu and C. Gao, *Adv. Mater.*, 2013, **25**(18), 2554.
36 X. Xu, Q. Zhang, Y. Yu, W. Chen, H. Hu and H. Li, *Adv. Mater.*, 2016, **28**(41), 9223.
37 I. Preibisch, P. Niemeyer, Y. Yusufoglu, P. Gurikov, B. Milow and I. Smirnova, *Materials*, 2018, **11**(8), 1287.